Biomaterials Advances 149 (2023) 213414

Contents lists available at ScienceDirect

Biomaterials Advances

journal homepage: www.journals.elsevier.com/materials-science-and-engineering-c

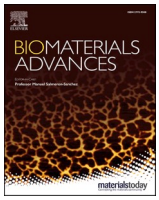

High resolution and fidelity 3D printing of Laponite and alginate ink hydrogels for tunable biomedical applications

Elena Munoz-Perez [a,b,1], Arantza Perez-Valle [a,b,1], Manoli Igartua [a,b,c], Edorta Santos-Vizcaino [a,b,c,*], Rosa Maria Hernandez [a,b,c,*]

[a] NanoBioCel Research Group, Laboratory of Pharmaceutics, School of Pharmacy, University of the Basque Country (UPV/EHU), Vitoria-Gasteiz, Spain
[b] Bioaraba, NanoBioCel Research Group, Vitoria-Gasteiz, Spain
[c] Biomedical Research Networking Centre in Bioengineering, Biomaterials and Nanomedicine (CIBER-BBN), Institute of Health Carlos III, Madrid, Spain

ARTICLE INFO

Keywords:
3D printing
Extrusion-based 3D printing
Ink
Laponite
Alginate
Biomedical devices

ABSTRACT

The formulation of hydrogels that meet the necessary flow characteristics for their extrusion-based 3D printing while providing good printability, resolution, accuracy and stability, requires long development processes. This work presents the technological development of a hydrogel-based ink of Laponite and alginate and evaluates its printing capacity. As a novelty, this article reports a standardizable protocol to quantitatively define the best printing parameters for the development of novel inks, providing new printability evaluation parameters such as the Printing Accuracy Escalation Index. As a result, this research develops a printable Laponite-Alginate hydrogel that presents printability characteristics. This ink is employed for the reproducible manufacture of 3D printed scaffolds with versatile and complex straight or curved printing patterns for a better adaptation to different final applications. Obtained constructs prove to be stable over time thanks to the optimization of a curing process. In addition, the study of the swelling and degradation behavior of the Laponite and alginate 3D printed scaffolds in different culture media allows the prediction of their behavior in future *in vitro* or *in vivo* developments. Finally, this study demonstrates the absence of cytotoxicity of the printed formulations, hence, setting the stage for their use in the field of biomedicine.

1. Introduction

The freedom of design and the automation of the manufacturing process offered by Extrusion-based 3D printing (EB3P) mark a clear future direction in the design and production of biomedical devices [1]. However, the adaptation of EB3P to the delicate process of obtaining biomedical formulations continues to be a challenge. The fabrication of printed biomedical devices with translational potential that could reach the market must ensure a robust, standardized and reproducible printing process. In this regard, obtaining inks with optimal physicochemical and biological characteristics that perform with high printing precision, accuracy and fidelity is critical. Among others, inks physicochemical characteristics should allow simple and non-interrupted extrusion, as well as shape maintenance and physical stability of printed constructs over time. Similarly, biological outcomes of the designed inks should enable construct biocompatibility and allow the versatile adaptation of the printed constructs to different biological environments. For such aim, the use of hydrogel-based inks is of great interest. Defined as hydrophilic porous matrices with high water content [2], hydrogels present high biocompatibility, are undoubtedly manageable and their composition can be precisely tailored to achieve different biological outcomes. Thus, the composition can be modified depending on the biological environment in which the printed constructs will be implanted, give rise to degradation profiles of different speed and present a drug release profile adaptable to the pathology to be treated. However, the optimization of hydrogels for their use in 3D printing is time consuming and requires great effort in technological development [1,3,4]. The groundbreaking evolution of this process is stacked with insufficient printing outcomes and poor printability results. Still, hydrogels are assumed to expand and collapsed when printed, hindering three-dimensional stacking of printed layers. The lack of standardized printing evaluation methods is delaying the advance and solution may

* Corresponding authors at: Laboratory of Pharmaceutics, School of Pharmacy, University of the Basque Country (UPV/EHU), Paseo de la Universidad 7, 01006 Vitoria-Gasteiz, Spain.
E-mail addresses: edorta.santos@ehu.eus (E. Santos-Vizcaino), rosa.hernandez@ehu.eus (R.M. Hernandez).
[1] Authors contributed equally to this work.

https://doi.org/10.1016/j.bioadv.2023.213414
Received 16 January 2023; Received in revised form 7 March 2023; Accepted 29 March 2023
Available online 5 April 2023

come with an effort of setting up a battery of specific printing tests that go further in detail, providing quantitative evidence of the quality of the printing process. Indeed, printing resolution, fidelity and reproducibility are not characteristics usually associated with the use of EB3P of hydrogels [1].

Even so, the softness and biocompatible characteristics of hydrogels makes them appealing for their application in EB3P techniques. Research on the composition of these materials has triggered a race for finding the best adaptation of the most widely used biocompatible polymers in the field of biomedicine to 3D printing technique [5,6]. Alginate (Alg) is one of the most investigated polymers in this regard [7,8]. Alg is considered one of the less harmful biomaterials and its usage is trustworthy [2]. As a great advantage, the curing of the Alg matrices can lead to their hardening, thus, stabilizing their physical integrity over time and easing their stackability [9]. However, the rheological profile of Alg hydrogels represents a limitation for its singly use in additive manufacturing. Thus, the softness of non-crosslinked Alg matrix as well as its low structural recovery after the printing processes, makes it necessary to implement composite materials with better rheological properties for the EB3P [10].

Interestingly, synthetic nanoclays such as Laponite (Lap) can be used as a support material for soft polymeric matrices [11,12]. Moreover, this nanoclay has demonstrated to be of interest for the design of biomedical formulations with an unrivaled adsorption capacity, tunable release profile and low risk of toxicity [13–15]. However, Lap is not usually employed as the main component of the designated formulations [16–18]. Thus, although having a robust structure that easily supports external forces is a characteristic sought in biomaterials, the stiffness of Lap matrices involve rheological challenges in most cases, hindering polymers flow when its concentration is overly high. In addition, the inability to apply curing processes in the manufactured constructs of Lap avoids obtaining stable solid printed forms over time and states as an important limitation for Lap single employment. For all this reasons, this material is usually discarded as the protagonist of formulated inks, generally being relegated to the background.

However, although Alg and Lap do not match the required characteristics for being used individually in 3D printing, the combination of both has proven to be of great interest [11,12]. The capacity of forming robust —non-breakable, stable and shapeable— printable matrices of Lap combined with the ability to maintain the shape of cured Alg matrices can lead to inks with good characteristics for EB3P [2,12]. Moreover, the combination of the biocompatibility of a well-known biomaterial such as Alg with the promising bioactive profile of the nanoclay for the development of useful biomedical devices states appealing. Among others, Laponite has been shown to have osteoinductive and hemostatic capacity, to be highly biocompatible and to give rise to biomedical devices with tunable drug release profiles and stimulus responsive behavior [19–21]. Up to now, rheological characteristics of this type of matrices have demonstrated their suitability for 3D printing [11,12]. Nevertheless, Lap concentration has a great impact on the behavior of the matrices and the appropriate composition of the matrices for EB3P has yet to be thoroughly evaluated. Moreover, there is still a frame to fill about the formulation, printability and biocompatibility characteristics of these Lap-Alg composite hydrogels.

In this article, we combined Alg and Lap to obtain printable hydrogels as well as shapeable and stable 3D printed constructs. First, as an indicative for optimal flow characteristics, an exhaustive rheological characterization of the composite hydrogels was performed. Remarkably, we proposed a quantitative standardizable procedure based on a well-designed battery of relevant tests for precisely selecting the ideal printing parameters of hydrogels as raw materials for EB3P. Moreover, we confirmed the optimal selection of printing parameters by describing the ability to create thick scaffolds, complex figures and custom-tailored infills with the designed ink. Besides, we provided a characterization of the proper crosslinking methods for the structural maintenance and mechanical resistance of the printed Lap-Alg scaffolds over time. Finally, we studied the biocompatibility of the constructs as well as we suggested their optimal culture conditions, study their swelling behavior and stability in different solutions and proposed a quick and controlled construct degradation method.

2. Materials and methods

2.1. Ink hydrogels preparation

Lap XLG® powder with an average particle size of ≤25 nm (Byk Additives & Instruments, Inc.) was dispersed in 6 mL of deionized water under gentle stirring. An ultraturrax dispersion system (J&K Ultra turrax T25) was then employed to homogenously disperse the ultrapure sodium Alg LVC (Novamatrix) containing a G/M ratio ≥ 1.5 and minimum 67 % of G monomers, 199 mPas viscosity and a 20–200 kDa Mw, until no sign of aggregates was observed. The ink hydrogel was then transferred into 3 mL luer-lock syringes and centrifuged at 3500 rpm during 15 min at room temperature to remove air bubbles. Five different ink gel compositions were prepared by keeping Alg concentration constant at 1 % (*w/v*) but varying Lap XLG® concentrations from 1.5 to 10 % (w/v). Thus, ink hydrogels were labelled according to their Lap XLG® composition as 1.5 % Lap-Alg, 4 % Lap-Alg, 6 % Lap-Alg, 8 % Lap-Alg and 10 % Lap-Alg.

2.2. Rheological characterization

The rheological characterization of the ink hydrogels was performed using a rheometer (TA instrument, Ar1000). A 40 mm diameter plate-plate geometry with a 600 microns gap was used to conduct the tests. Steady-state shear viscosity measurements of all hydrogels were performed in a range of 1 to 1000 s^{-1} of shear-rate. Then, an amplitude sweep test was accomplished to determine the linear viscoelasticity (LVE) range of the ink hydrogels. An angular frequency of 10 rad×s^{-1} was set stable while storage modulus (G′) and loss modulus (G″) were tested in a shear strain rate of 1 to 4 %. Next frequency sweep tests were carried out at a selected constant shear strain within the LVE range and frequency rates from 0.06 to 627 rad×s^{-1}. The damping factor — tan (δ) — was subsequently calculated as: (Eq. (1)).

$$tan\delta = \frac{G''}{G'} \tag{1}$$

Finally, structure recovery of the best performed ink hydrogel composition was tested in a modulus recovery test where low and high shear strain cycles were combined over time and G′and G″ changes were observed. All rheological characterization tests were performed in triplicate.

2.3. Filament formation test

Filament formation test was performed using an extrusion-based 3D printer (Bio X, Cellink) with 3 mL pneumatic cartridges and a 22G nozzle. The minimum extrusion pressure (MEP) required for the flow of each ink hydrogel composition was employed for the test. Ink hydrogels with better filament formation conditions and most suitable rheological profiles were selected for further studies.

2.4. Extrudability assay

The extrudability assay was performed using a mechanical tester (TA.XT plusC, TA systems) with a 50 N load-cell. Briefly, the selected ink hydrogels were put in 3 mL luer-lock syringes and placed in an elevated fixable platform. Syringe embolus were pushed at a compressive rate of 0.5 mm × s^{-1}. The force needed for the displacement of 15 mm of ink hydrogel was recorded within different cylindrical nozzle diameter of 22, 25 and 27G for each of the tested ink hydrogels. Force stability within the tests was considered an indicator of homogeneity and as an

improvement of the printing parameters.

2.5. Printability assessment

The optimization of the parameters for the EB3P of the formulated hydrogel was studied employing ink-loaded 3 mL cartridges and a 22G nozzle at room temperature (21–24 °C).

2.5.1. Filament deposition test in 2D models

2D models with seven segments of 12 mm length were designed in AutoCAD. This design was printed over glass slides varying pressure, speed and nozzle geometry (Table 1). Each printed model geometry was analyzed in Image J software (NIH).The first segment of the model was used as extrusion stabilization brim and was not analyzed. The printed length of each segment and width at the beginning, middle and end of each segment was calculated.

2.5.1.1. Deposition accuracy (DA). In the printed 2D models, the length of the six printed segments was calculated and compared to the computer design (12 mm) in each printing condition (Eq. (2)). The closer the ratio to 1, the more accurate the printing process.

$$\mathrm{DA} = \frac{\text{Printed strand length}}{\text{Design length}} \tag{2}$$

2.5.1.2. Spreading ratio (SR). To select the optimum parameters, the spreading ratio for each condition was studied in 2D designs as described before [22]. The mean (beginning, middle and end) of the printed filament width was calculated in the six segments of the model and related to the inner diameter of the needle (0.41 mm) (Eq. (3)). The closer the ratio to 1, the more accurate the printing process.

$$\mathrm{SR} = \frac{\text{Printed strand width}}{\text{Needle inner width}} \tag{3}$$

2.5.1.3. Parameter optimization index (POI). The final optimization of the printing parameters in 2D simple designs has been performed applying the equations (Eqs. (4) and (5)) [23].This enables the identification of the best combination of pressures, nozzle gauges and printing speeds for the given ink. The POI_i (Eq. (4)) for a sweep of parameters for the same ink can be expressed as:

$$\mathrm{POI_i} = \frac{1}{t_{line}.D_G.\rho} \tag{4}$$

Then, to select the best parameter combination, each POI_i can be normalized to the higher POI detected (POI_{MAX}) in the experimental set up (Eq. (5)). The final POI values can vary from 1 (the best) to 0 (the worst).

$$\mathrm{POI} = \frac{\mathrm{POI_i}}{\mathrm{POI_{MAX}}} \tag{5}$$

2.5.2. 3D scaffold printing

5- and 15-layer square lattice constructs were printed with a rectilinear infill. The dimensions of the computer-designed geometries were 12 × 12 mm squares with 2.05 mm —5 layer construct— and 6.15 mm —15 layer construct—. The 3D geometries were printed with the previously optimized parameters: 2 mm/s speed, 75 kPa pressure with 22G cylindrical nozzle at room temperature.

Table 1
Description of the different parameter combinations employed in the printing of 2D designs.

Caliber and nozzle type	Printing pressure (kPa)	Printing speed (mm/s)
22G conical	30 to 55	1 to 4
22G cylindrical	70 to 90	1 to 4

Measurement of 8 pores per construct were employed for the study of the printability index and pore diffusion rate. The rest of the below described parameters were measured in 20 replicate scaffolds in fresh and after curation process. Briefly, for curation, constructs were submerged in a 100 mM $CaCl_2$ solution for 10 min.

2.5.2.1. Printability index (Pr). The printability of the inks can be related to the ability to create square-shape internal pores in the printed geometries. With the printability index (Eq. (6)), the perfect square shape pores yield a value of 1.

$$Pr = \frac{\text{Printed perimeter}^2}{16 \text{ x Printed area}} \tag{6}$$

2.5.2.2. Pore diffusion rate. Pore diffusion rate measures the ability to create perfect internal pores (Eq. (7)). The closer to 0, the more similar to the computer design. $Area_D$ represents the area of the pores of the design, while $Area_P$ is the area of the printed pores.

$$\text{Pore Diffussion Rate} = \frac{\mathrm{Area_D} - \mathrm{Area_P}}{\mathrm{Area_D}} \tag{7}$$

2.5.2.3. Printing Accuracy Escalation Index (PAEI) (length, height). To determine if the 2D printing accuracy is scalable to 3D complex designs using the same printing conditions, a new index has been defined. Here, the filament height and length printed in 2D was related to the height and length obtained in the 3D printed and crosslinked scaffolds (Eq. (8)). The closer the index to 100, the higher the printing fidelity is between 2D and 3D designs.

$$\mathrm{PAEI} = \frac{\text{2D Printed length}_{X,Z}}{\text{3D Printed length}_{X,Z}} \times 100 \tag{8}$$

2.5.2.4. Geometrical Printing Irregularity Index (PII) (length, perimeter, height). The outer geometrical irregularities in any direction between the 3D printed scaffold and the computer design were calculated applying the Irregularity Index. For this, the length in X, Y or Z directions of the printed and crosslinked scaffolds were related to the outer geometry of the computer-design (12 × 12 × 2.05 mm) (Eq. (9)). The closer the PII to 100, the closer to the computer design.

$$\mathrm{PII} = \frac{\text{Printed length}_{X,Y,Z}}{\text{Design lentgh}_{X,Y,Z}} \times 100 \tag{9}$$

2.5.2.5. Deflection ratio. The deflection of a printed strand is another imperfection noticed and accounts for structural integrity. For this, the area of the printed scaffold is related to the computer-design area (48 mm^2) as described before [24] (Eq. (10)). The closer the ratio to 100, the more similar the printed and designed area are.

$$\text{Deflection Ratio} = \frac{\text{Printed area}}{\text{Design area}} \times 100 \tag{10}$$

2.5.2.6. Printing accuracy. The area of the printed and crosslinked scaffolds were compared to the computer-design area (48 mm^2) to determine the accuracy of the printing process [25] (Eq. (11)). The closer the result to 100, the higher the printing accuracy of the process.

$$\text{Printing Accuracy} = \left[1 - \frac{(\text{Printed area} - \text{Design area})}{\text{Design area}}\right] \times 100 \tag{11}$$

2.6. Mechanical characterization of printed constructs

A mechanical tester (TA.XT plusC texture analyzer, TA systems) with a 50 N load-cell at a compressive rate of 0.5 mm × s^{-1} up to 60 % strain was used to perform a single-cycle compression test. The test, was applied using a 20 mm probe to the printed constructs crosslinked with

$CaCl_2$ (100 mM) up to 5, 10, 20 and 60 min ($n = 3$). Different printed constructs (n=3) were analyzed for each of the tests in order to prove the reproducibility of the mechanical properties between different batches. The tangent modulus was calculated at the maximum stress value of each of the stress-strain curve and employed to compare the influence of the crosslinking time on the mechanical characteristics of the printed construct.

2.7. Swelling and degradation profile

2.7.1. Degradation profile

After the crosslinking of the 5-layer constructs by submerging the constructs in a $CaCl_2$ 100 mM solution for 10 min, they were weighed and incubated in the shaker at 37 °C at different conditions: 1) complete culture media: DMEM (ThermoFisher Scientific); 2) PBS without Ca^{+2} and Mg^{+2} (ThermoFisher Scientific) -; 3) H_2O milliQ; 4) 100 mM $CaCl_2$ in H_2O for 10 min; 5) 1 % EDTA in PBS w/o Ca^{+2} and Mg^{+2} (*w/v*); or 6) 0.5 mg/mL Alg Lyase in PBS w/o Ca^{+2} and Mg^{+2} (#A1603, Sigma-Aldrich) ($n = 3$). After 30 min, these scaffolds were again weighed and the differences in the weight percentage at each time-point ($Weight_i$) were calculated compared to the crosslinked scaffold ($Weight_{0h}$) (Eq. (12)).

$$\text{Weight } (\%) = \frac{\text{Weight}_i}{\text{Weight}_{0h}} \times 100 \tag{12}$$

2.7.2. Swelling profile

The 5-layer constructs were crosslinked and weighed. Then, the constructs were incubated in: 1) Complete DMEM; 2) PBS; 3) H_2O milliQ; or 4) 100 mM $CaCl_2$ ($n = 4$), and weighed at time-points 30 min, 1 h, 2 h, 6 h, 24 h and 48 h. The differences in weight percentage at each time-point ($Weight_i$) were calculated related to the printed scaffold for each culture condition ($Weight_{0h}$) (Eq. (12)).

2.8. Dimensional stability over time (length, height)

The dimensional stability over time of the constructs used for studying the swelling profile was studied by measuring their outer geometry (length and height). At each time point, the printed ($length_i$) and computer design ($length_d$) were compared (Eq. (13)).

$$Dimensional\ stability = \frac{Length\ i_{X,Z}}{Length\ d_{X,Z}} \times 100 \tag{13}$$

2.9. Cytotoxicity assay

Cytotoxicity of the constructs was evaluated according to the ISO 10993-5:2009 guidelines. Thus, viability of L-929 fibroblasts (ATCC® 30-2003™) was assessed both by indirect and extract contact. Absorbance was determined with a plate reader (Infinite® 200 PRO series, Tecan Trading AG) at 450 nm after 2 h of exposure of the CCK reagent with cells. A wavelength reference of 650 nm was employed for the measurement. Cells not exposed to the constructs were used as a control group (100 % viability) and cells in contact to a 10 % Dimethyl sulfoxide (DMSO) EMEM solution were employed as a death control group (0 % viability).

In the indirect cytotoxicity assay, 35,000 L929 cells per well were seeded in a 24-well plate using 500 μL/well of EMEM (Thermo Fisher) complete medium. After an incubation period of 24 h at 37 °C, medium was discarded and refreshed, and the scaffolds were placed in indirect contact with cells using a transwell ($n = 6$ samples per group). After 24 h and 48 h of incubation, the media was replaced with 300 μL of CCK-8 (Sigma Aldrich) and after 2 h of incubation the viability was measured.

To carry out the extract cytotoxicity assay, each 100 mg of construct was lixiviated for 24 h in 1 mL of fresh EMEM medium. Cells seeded at a concentration of 5,000 cell/well in 96-well plate were exposed to 100 μL of the obtained construct lixiviate and incubated for 48 h. Cell viability measurements were made at 24 h and 48 h incubating cells with 100 μL of CCK-8 for 2 h. Lixiviated EMEM medium was employed as a control group.

A live/dead staining (Fisher scientific) was performed at 48 h to prove visual data of L929 cell viability. An epi-fluorescence microscope (Nikon) equipped with a DSD2 confocal modulus was employed in order to capture visual signal of cells.

2.10. Statistical analysis

One-way ANOVA was employed to analyze normally distributed results. A Bonferroni or Tamhane post-hoc analysis was applied based on the homogeneity of variances Levene's test. Non-normally distributed values were analyzed by Mann-Whitney's analysis. Results were expressed as the mean ± SD. Statistical analysis was performed using SPSS 25.0 (SPSS®) and $p < 0.05$ was considered statistically significant.

3. Results

3.1. Rheological characterization

As it can be observed in the Fig. 1A, marked shear-thinning behavior was demonstrated in all the tested formulations. The highest initial viscosities were observed for the 10 % Lap-Alg and 8 % Lap-Alg formulations. In order to test the viscoelastic behavior of the formulations, oscillatory shear tests were performed. First, the LVE range was defined in an amplitude shear test at a constant angular frequency of 10 rad×s^{-1} (Supplementary Fig. 1). A strain of 1 %, shown to be within the LVE range was fixed stable to perform an oscillatory frequency sweep test. As shown in Fig. 1B, G′ was maintained above G″ and stable for all the tested compositions. Moreover, tan (δ) values were consistent with a solid-like behavior for all of the tested formulations — tan (δ) < 1 — Fig. 1C. Noticeable differences in the rheological profiles were observed at low angular frequencies in 1.5 % Lap-Alg and 4 % Lap-Alg formulations while tan (δ) proved to be more stable for 6 % Lap-Alg, 8 % Lap-Alg and 10 % Lap-Alg.

3.2. Filament formation test

As shown in Fig. 1D,E, straight filament formation is only observed in the 6 % Lap-Alg hydrogel. The MEP — minimum extrusion pressure — was higher for 6 % Lap-Alg, 8 % Lap-Alg and 10 % Lap-Alg compared to that required for the extrusion of 1.5 % Lap-Alg and 4 % Lap-Alg. These results combined with the rheological characterization of the tested hydrogels composition confirm that 6 % Lap-Alg, 8 % Lap-Alg and 10 % Lap-Alg were the hydrogels with better printing characteristics. Therefore, further printing parameters optimization studies were performed on these hydrogels.

3.3. Extrudability assay

As shown in the mechanical tester results forces required for the extrusion of hydrogels 8 % Lap-Alg and 10 % Lap-Alg were higher than those required for the extrusion of 6 % Lap-Alg hydrogels (Fig. 1F). In terms of force stability, 8 % Lap-Alg and 10 % Lap-Alg hydrogels reflected marked peaks among their test curves, which were less noticeable in 6 % Lap-Alg. According to the variability produced by the nozzle calibers tested in the assay — 22, 25 and 27G —, an increase in the extrusion force required was sought for nozzle calibers of 25 and 27G among all of the hydrogel compositions tested. Notably, the lower extrusion force and the most stable force curve was observed for 6 % Lap-Alg hydrogels extruded through the nozzle caliber of 22G. Thus, according to the rheological suitable profile, promising filament formation test performance and demonstrated optimal extrudability, 6 % Lap-Alg hydrogel was selected as the ink composition for further

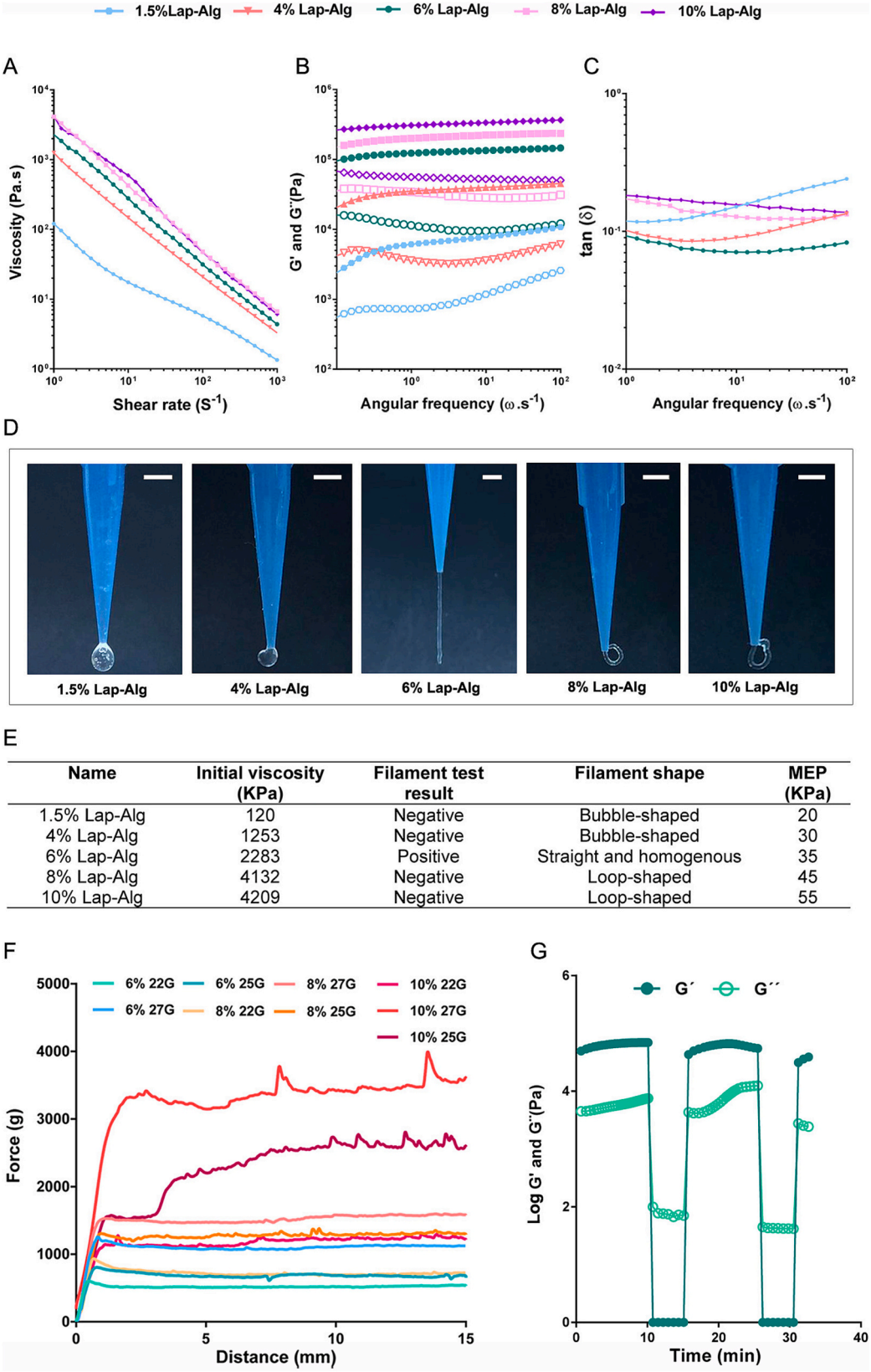

E

Name	Initial viscosity (KPa)	Filament test result	Filament shape	MEP (KPa)
1.5% Lap-Alg	120	Negative	Bubble-shaped	20
4% Lap-Alg	1253	Negative	Bubble-shaped	30
6% Lap-Alg	2283	Positive	Straight and homogenous	35
8% Lap-Alg	4132	Negative	Loop-shaped	45
10% Lap-Alg	4209	Negative	Loop-shaped	55

Fig. 1. Rheological and mechanical characterization of Lap-Alg hydrogels. (A) Flow test. (B) Frequency sweep test G′ (solid symbols) and G″(open symbols). (C) Damping factor (D) Filament flow test. Scale bar: 1 mm. (E) Summary table including initial viscosity profiles of hydrogels. Positive or negative filament formation is specified and the minimum extrusion pressure (MEP) for the formation of each filament is displayed (F) Extrudability test results. (G) Recovery rheological assay for the 6 % Lap-Alg ink hydrogel.

printability assays. Additionally, appropriate nozzle caliber was stated in 22G.

3.4. Recovery assay

In order to test their shape maintenance capacity, a recovery rheological test was next performed on the selected 6 % Lap-Alg hydrogel

(Fig. 1G). Remarkably, initial G′ and G″ modulus of the hydrogel were recovered after high shear strain cycles. Moreover, the capacity of the formulation to switch easily from a solid-like behavior — G′ > G″ — to a liquid-like behavior — G′ < G″ — and to recover to its initial solid-like structure was reflected in the assay results.

3.5. Optimization of printing parameters in 2D filaments

2D strand printability with 22G cylindrical and conical nozzles was analyzed by comparing the computer design with the printing precision and accuracy obtained in 44 combinations of varying printing pressures and speeds (Supplementary Table 1, Fig. 2A). First, in each segment of the model, the deposition accuracy and precision of the prints were studied based on the length (Supplementary Tables 1, 2; Fig. 2B,C;

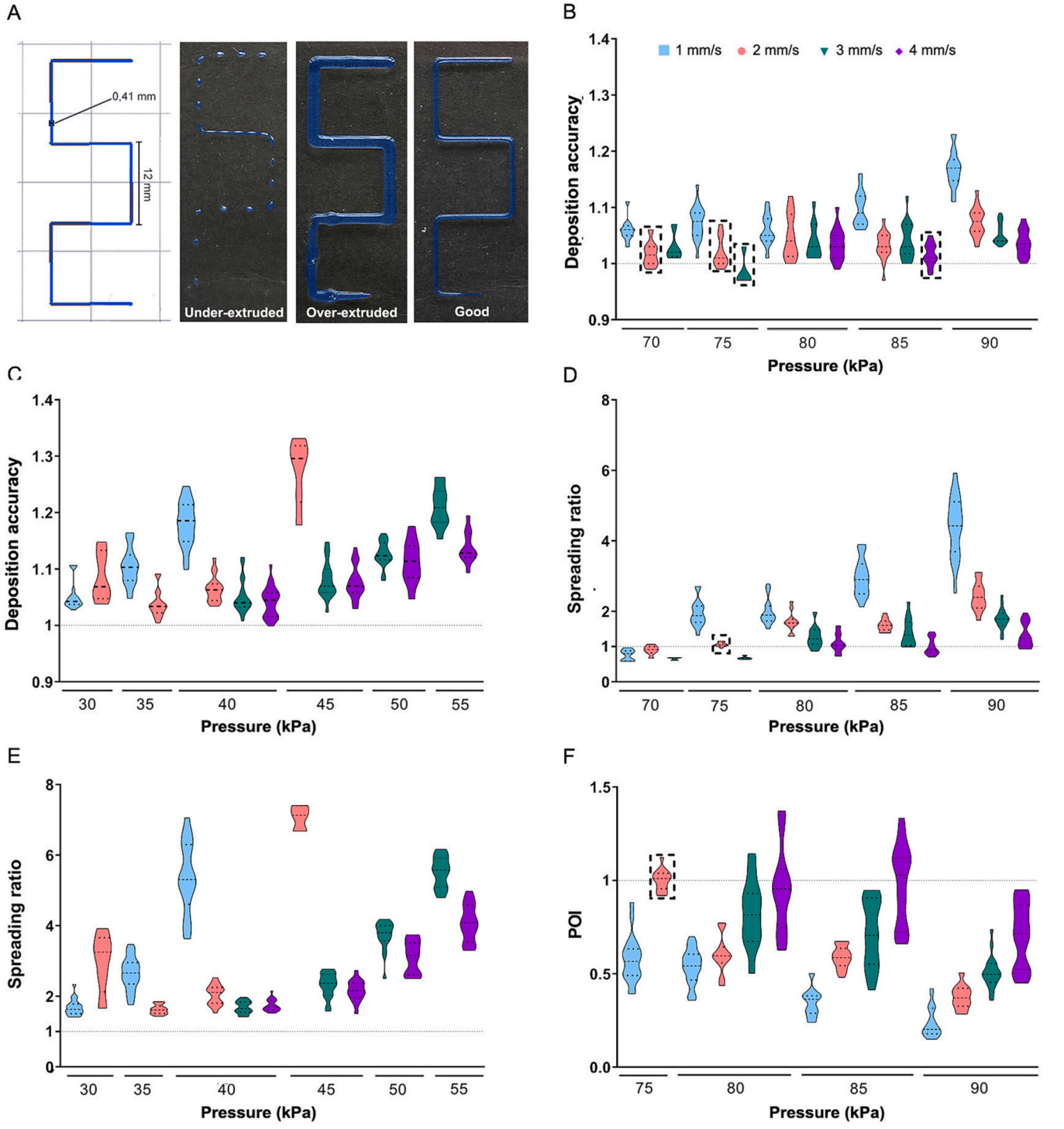

Fig. 2. Printing parameters optimization in simple 2D designs. (A) 2D computer model for printability assessment and different printing outcomes at varying conditions. Deposition accuracy and spreading ratio at the different printing conditions with cylindrical (B and D) and conical nozzles (C and E). (F) POI studies in a range of printing conditions with cylindrical nozzles. Data are presented in violin plots showing median and 25th and 75th quartiles to observe the distribution of the results. The boxes around specific data sets denote the selected parameters.

Supplementary Fig. 2A). Both in the cylindrical and conical nozzles, there is great precision with a coefficient of variation lower than 5 % between the replicates of each condition. Regarding the deposition accuracy, the most accurate conditions were selected as the ones that their length differs less than a 2.5 % from the design length (DA: 1.000 ± 0.025). Here, only four combinations printed with the cylindrical nozzle were selected as the most precise and accurate based on the printed lengths: 2 mm/s: 70 and 75 kPa; 3 mm/s: 75 kPa; 4 mm/s: 85 kPa).

Among the conditions filtered by the printing precision and accuracy in the length, the combinations with the best shape fidelity according to the strand width and spreading ratio were chosen. Here, two conditions printed with the cylindrical nozzle were chosen with the lowest variation in the width of their strands (CV: <7 %), confirming good uniformity: 2 mm/s - 75 kPa, and 3 mm/s - 75 kPa (Supplementary table 1; Fig. 2D/E; Supplementary Fig. 2C/D). The spread of the strands after the deposition in the printing surface and their similarity to the design were also considered – *i.e.* spreading ratio—. Here, the condition with the lowest spread was selected: 2 mm/s - 75 kPa printed with the cylindrical nozzle. This was, after filtering all the analyzed printing parameters, considered the most precise and accurate condition (Spreading Ratio: 1.000 ± 0.063). (Supplementary Table 1; Fig. 2D).

The POI correlates the parameters that maximize the printing accuracy and minimize the shear stress of the ink. Considering the over-extrusion observed in conical nozzle, only the strands printed with cylindrical nozzle were analyzed. Besides, the conditions printed with the cylindrical nozzle at 70 kPa at every printing speed, and 75 kPa at 3 and 4 mm/s were not considered for this test since the strands were under-extruded and presented gaps. The results here obtained confirm that the best combination of printing parameters for the optimized Lap-Alg ink is 2 mm/s - 75 kPa extruded with cylindrical nozzle (Supplementary Table 1; Fig. 2F).

3.6. Printability assessment of 3D scaffolds

The parameters set in 2D designs (22G cylindrical nozzle, 2 mm/s and 75 kPa) were used to study the printability, by analyzing the inner geometrical structure of the 5- and 15-layer scaffolds. The obtained results expose a Printability Index (Pr, Eq. 6) very close to 1 in both cases with a high precision and accuracy, confirming the capacity of creating square-shape pores especially in the center of the constructs (Fig. 3A/B). Moreover, the results demonstrate that the formed pores are similar to the computer design (Eq. (7), Fig. 3C), highlighting that good printability outcomes are also achieved in 3D scaffolds.

3.7. Mechanical characterization of constructs

The influence of the crosslinking time on the mechanical behavior of the constructs was tested in single-cycle compression test (Fig. 4**).** The compressive stress at a strain of 60 % is the lowest for the non-crosslinked constructs (Fig. 4A**);** in contrast, the stress reached for all of the crosslinked constructs was notably higher. Notably, differences within replicative curves for the non-crosslinked and the 5 min crosslinking time were more noticeable in comparison to the close reproducibility of the replicated curves values for the rest of the crosslinking times Fig. 4B,C,D,E. Moreover, stress-strain curves were similar for crosslinking times of 10, 20 and 60 min. Likewise, tangent modulus was significantly higher for crosslinking times of 5, 10, 20 and 60 min in comparison to non-crosslinking time **(**Fig. 4F**).** Non-significant differences were demonstrated in the tangent modulus between 10, 20 and 60 min. However 5 min crosslinking of constructs showed to have lower tangent modulus, non-reaching a plateau and stating 10 min as the minimum sufficient crosslinking time for the stabilization of the stiffness.

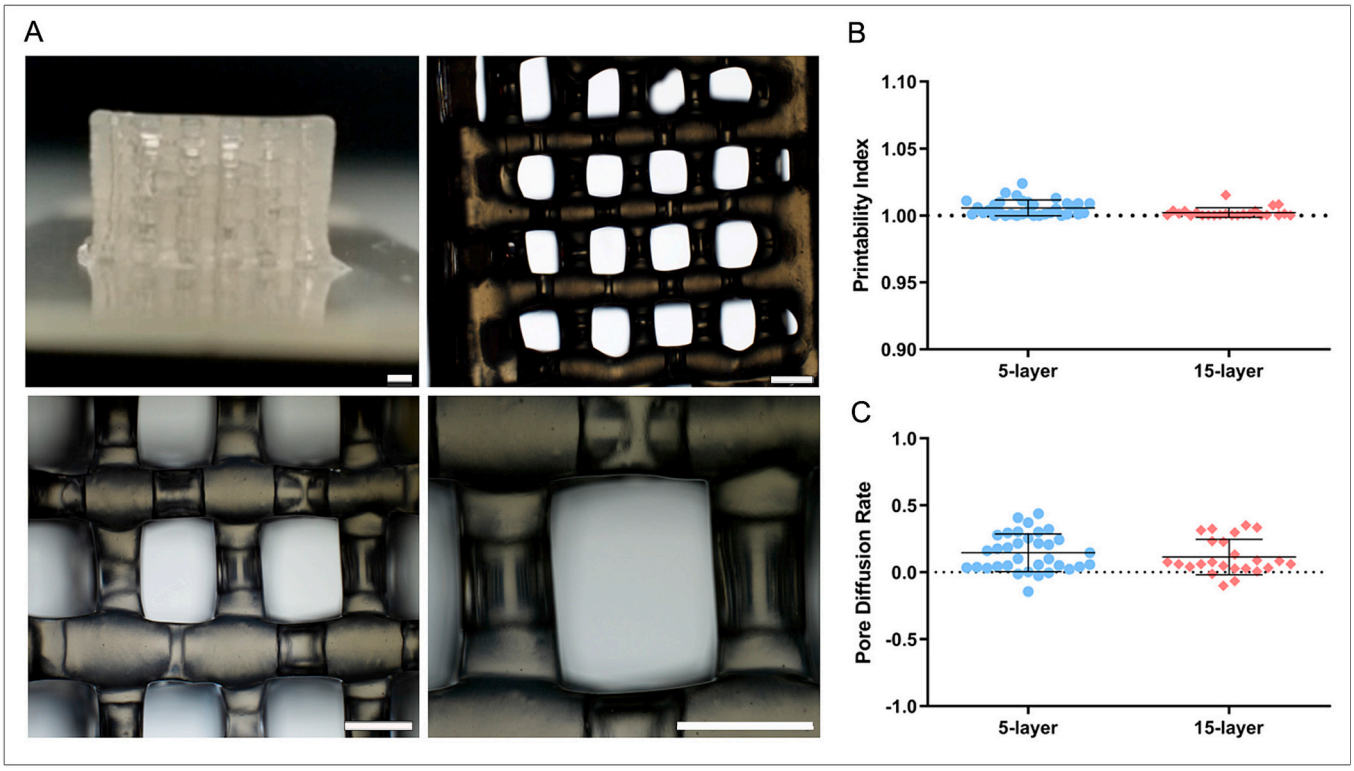

Fig. 3. Printability evaluation of 5- and 15-layer constructs. (A) Pictures of a 15-layer constructs. Scale-bar: 1 mm. Analysis of the printability index (B) and pore diffusion rate (C) in 5- (blue) and 15-layer constructs (red).

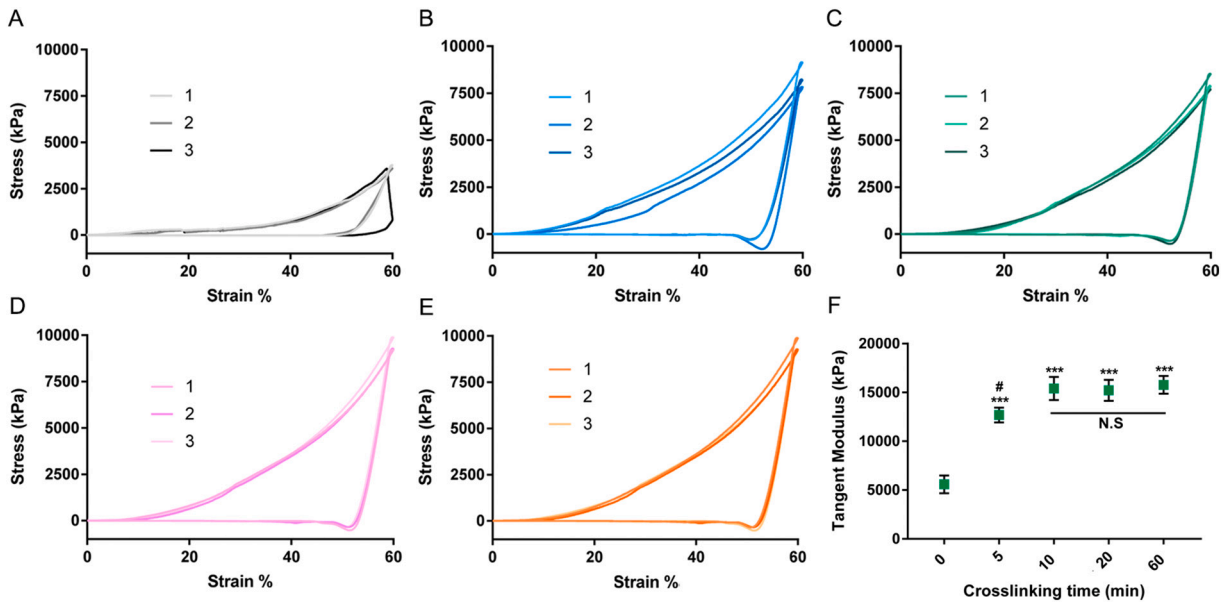

Fig. 4. Mechanical characterization of crosslinked 3D printed constructs. (A) Stress-strain curves for different crosslinking times: (A) 0 min, (B) 5 min, (C) 10 min, (D) 20 min, (E) 60 min. (F) Tangent modulus comparison among different crosslinking time (* represents comparison against 0 and 5 min crosslinking time groups; $p < 0.05$ *, $p < 0.01$ **, $p < 0.001$ ***; # represents comparison against 10, 20 and 60 min crosslinking time groups; $p < 0.05$ $^{\#}$, $p < 0.01$ $^{\#\#}$, $p < 0.001$ $^{\#\#\#}$).

3.8. Printing outcomes of fresh and crosslinked 3D scaffolds

First, we analyzed if the printing accuracy achieved with the set parameters in 2D designs were scalable to 5-layer square lattice 3D constructs (PAEI, Eq. (8)). The results show that very high accuracy and precision is maintained in the length and height of both fresh and crosslinked scaffolds. In addition, the printing is highly reproducible as the low coefficients of variation show (all CVs <9 %) (Supplementary Table 3; Fig. 5A).

Next, the outer geometry of the printed and crosslinked scaffolds was related to the design (PII, Eq. (9)). The results demonstrate that there is a very high shape fidelity, especially according to the length and perimeter of the square. In fact, after crosslinking, the scaffolds presented a shape fidelity very close to 100 % (Supplementary Table 3; Fig. 5B).

Additionally, here we demonstrate that the actual and theoretical area of our scaffolds (48 mm^2), especially after the crosslinking process, are very close to the design value (**Eq. 10; Supplementary Table 3;** Fig. 5C**).** Markedly, the printing accuracy of the Lap-Alg ink with the set printing parameters is of 100 % after crosslinking the scaffolds (**Eq. 11; Supplementary Table 3;** Fig. 5D). As seen in Fig. 5E the printed constructs present uniform filaments and the formed pores maintain their square shape-.

The excellent printing outcomes achieved in the previous results enable the printing of complex designs with high resolution, precision and accuracy (Fig. 6). The infill commonly used in 3D printing is a simple pattern formed with continuous and straight strands. Nevertheless, other patterns can be printed such as concentric (Fig. 6AI, V), wave (Fig. 6BAII, VI), honeycomb (Fig. 6BAIII, VII) and tri-hexagons (Fig. 6BAIV, VIII). In the same way, we have printed a highly complex 3D design, the logotype of the University of the Basque Country (UPV/EHU), which confirms the high printing resolution, precision and accuracy achieved with this Lap-Alg ink (Fig. 6B).

3.9. Degradation/swelling profile and dimensional stability of 3D printed hydrogels

The fastest degradation was achieved in 30 min by incubating the constructs with EDTA in PBS (Fig. 7A). On the contrary, the employment of Alg lyase in PBS against the Alg chains of the structure did not show any effect, as well as, culture media and H_2O miliQ. Regarding the swelling assay, in the first 24 h of incubation, there is a de-swelling in every condition tested. The loss of weight is more pronounced in PBS than in culture media (Fig. 7B). Thereafter, the scaffolds in culture media and H_2O swell and increase their weight, the scaffolds in $CaCl_2$ keep losing weight and in PBS they are completely disintegrated after 48 h of incubation.

As shown in Supplementary Fig. 3, although there is an initial decrease in the perimeter and the height of the scaffolds, the dimensional stability of these is maintained over time. In addition, the images of the internal pores of the different scaffolds confirm that only PBS scaffolds are degraded (Fig. 7C).

3.10. Cytotoxicity evaluation

As presented in Fig. 8**,** indirect exposure of L929 fibroblasts to the construct-lixiviated medium did not have a negative impact on cell viability. Both, the positive control group and the scaffold treated group showed a viability above 70 %. Remarkably, biocompatibility was maintained after 48 h of exposure. Similarly, indirect transwell mediated exposure of cells to the construct was not harmful eliciting cell viabilities above 70 % in 24 and 48 h after the exposure (Fig. 8C). Biocompatibility of the constructs was also visually proved with the Live/Dead staining (Fig. 8B, D) on which practically all of the cells exposed to the constructs or lixiviated medium showed to be alive—green colored — after 48 h of exposure.

4. Discussion

To date, the exploration of Alg and Lap combination for extrudable hydrogel formation has elucidated the limitations that these components offer to the process. Thus, the concentrations of both compounds, as well as the ionic charge of the dispersion medium used for the formation of the inks have proven to be of great importance. More specifically, concentrations >1 % of Alg have been shown to hinder the extrusion of formulations, leading to easy formation of aggregates and high viscosity increase. Moreover, concentrations above 6 % (*w/v*) of Lap have not been tested in combination with Alg without defining an upper concentration limit. Similarly, low concentrations —below 1 %

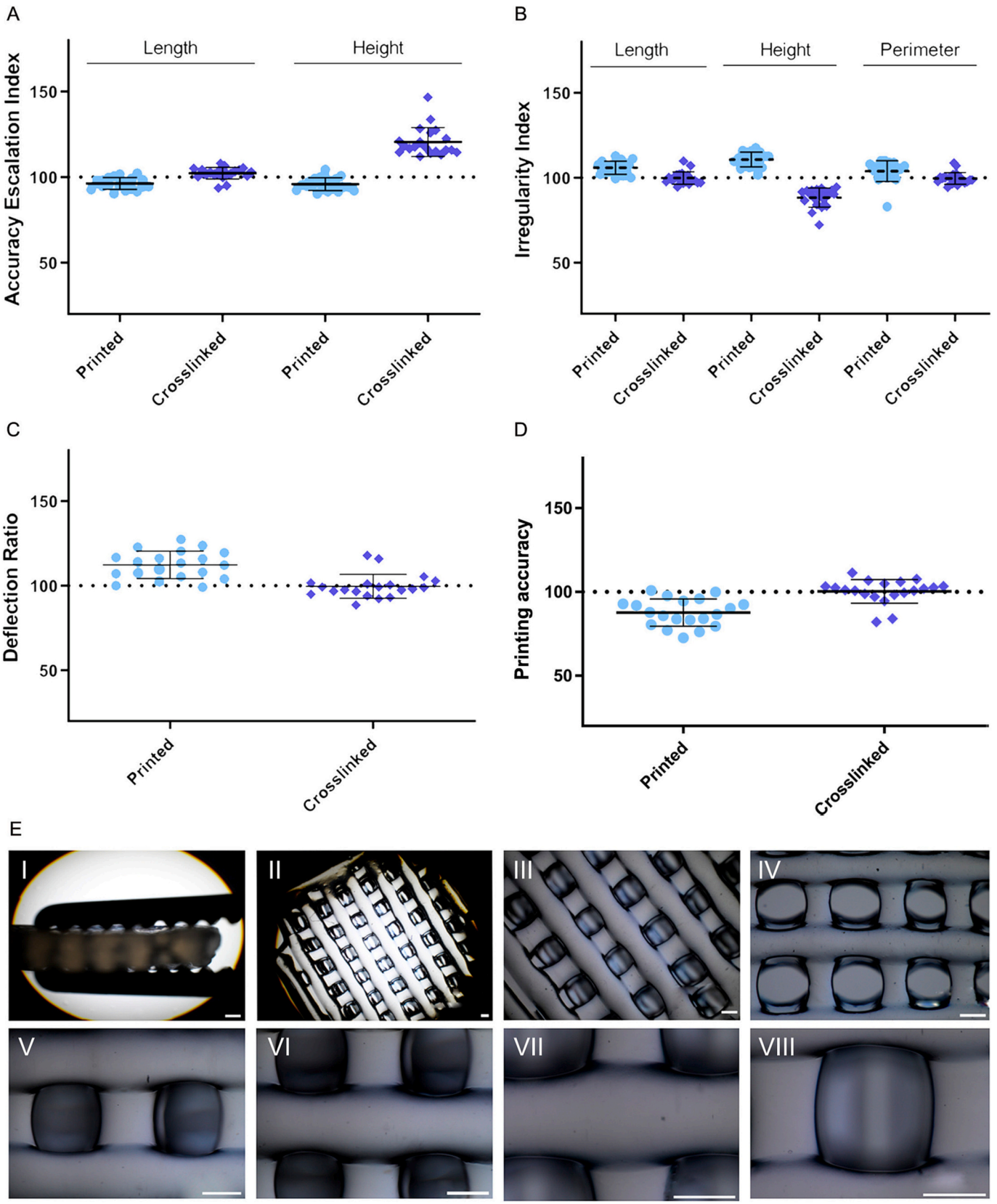

Fig. 5. Study of the printing outcomes in fresh and crosslinked 5-layer constructs. Evaluation of the PAEI (A), PII (B), Deflection Ratio (C) and Printing Accuracy (D) in fresh (light blue) and crosslinked (dark blue) 5-layer scaffolds. (E) 5-layer constructs at different magnifications (I – 1×; II – no magnification; III – 2×; IV – 3×; V and VI – 4×; VII – 5×; VIII – 6×). Scale-bar: 500 μm.

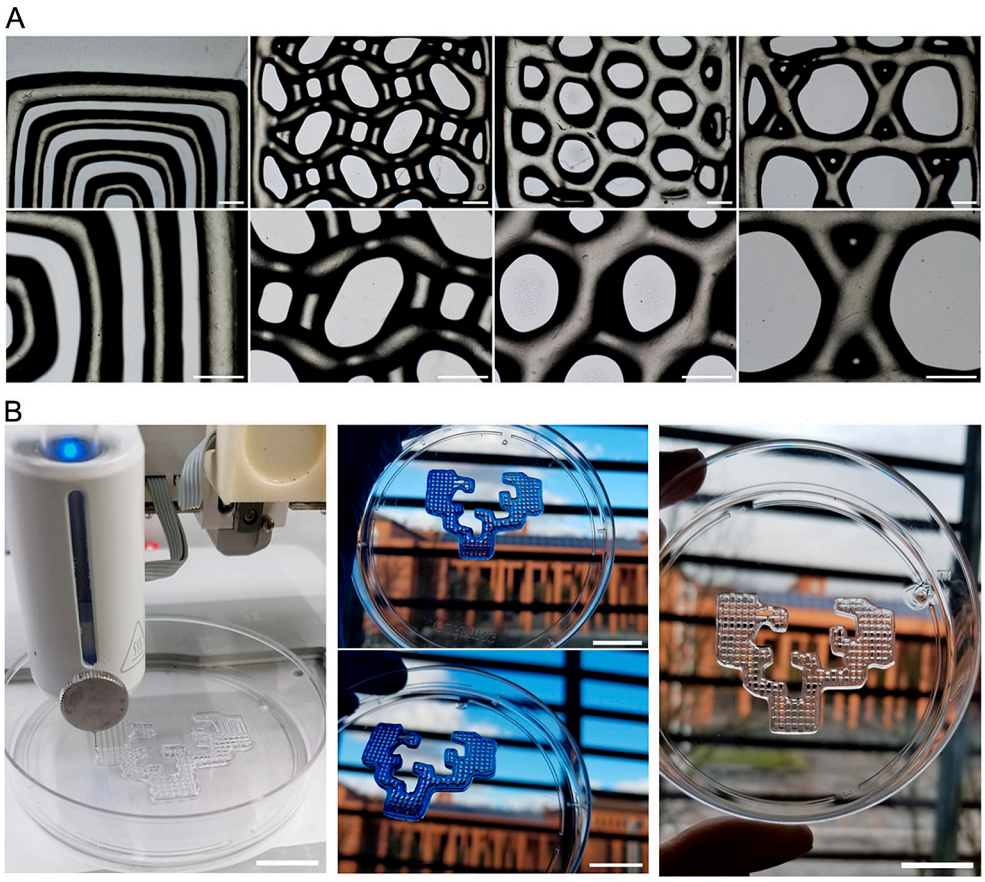

Fig. 6. 3D printing of complex designs. (A) Square 3D constructs printed with different infill designs: concentric (I/V), waves (II/VI), honeycomb (III/VII), trihexagons (IV/VIII). Scale bar: 1 mm. (B) 3D printing of the complex logotype of the University of the Basque Country (UPV/EHU). Scale bar: 2 cm.

(w/v) for Alg and 2 % (w/v) for Lap— of both components have demonstrated to hinder the formation of the matrix [11,12]. Regarding the influence of the ionic charge, the sensitivity of both components to high ionic forces affects the formation of the matrix. Therefore, a controlled ionic environment is strictly necessary for the formation of the Lap-Alg formulations and their optimal handling.

Rheological studies confirmed Lap-Alg hydrogels as shear thinning behavioural inks pointing hydrogels with 6 % or more of Lap as solid-like stable matrices. Solid-like behavior stability was not maintained through angular frequency variations for the rest of formulations, pointing unstable interactions between Lap and Alg. However, despite the fact that rheological studies provided a clear profile on the flow characteristics of hydrogels, we evaluated the behavior of the formulations within studies related to variables inherent to the actual printing process [26,27]. Appearance of drops at the tip of the nozzle is usually attributed to a low consistency of the inks; on the contrary, inks that are too consistent can lead to nozzle-attached loops [28,29]. Therefore, optimizing the extrusion parameters, ink homogeneity or the tip caliber, can condition the formation of these filaments [30,31]. As can be observed in our study, force oscillation within the extrudability assay can be directly related to the presence of aggregates or bubbles in the tested hydrogels, as observed for the 8 % Lap-Alg and 10 % Lap-Alg formulations [32].

Thus, the designed characterization study stated 6%Lap-Alg hydrogel as the most suitable one for printing and shaping eliciting great results in recovery assay and demonstrating to perform excellent bulk recovery. These characterization results could be correlated with the subsequent internal structure in our hydrogels. Thus, a simple ionic interaction model can be proposed where the electrostatic bonds between Lap plates and Alg chains occur. More accurately, negatively charged Alg chains may interact with Lap's positively charged rims leading to entangled matrices. This structure would remain stable under hydrogel rest conditions — when they rest in the printing cartridge— (Fig. 9A) [11]. Disentanglement of the matrix and plate orientation in favor of the flow direction —when printing pressure is applied— would allow hydrogel extrusion to happen easily (Fig. 9B) [32–34]. Finally, hydrogel matrix structure would recover immediately after printing allowing printed constructs' shape maintenance and stacking. Printing process finished, the cure of constructs with $CaCl_2$ would provide ionic crosslinking of Alg chains and construct hardening. In addition, Lap platelets would assemble with the Alg chains reinforcing the structure. (Fig. 9C). Thus, the stability of the structure of the hydrogel formed is based not only on the incorporation of Laponite into the system, but also, and crucially, on the sodium alginate chosen for the formulation of the matrix. The low molecular weight of the chosen alginate gives the hydrogel a low initial viscosity, facilitating its extrusion and its shear-thinning capacity. This controlled viscosity of the alginate matrix allows us to modulate the flow of the designed hydrogel through the rest of the formulation components while providing mechanical stability. Notably, Ca^{2+} ions selected for the crosslinking of constructs elicits the "egg-box" crosslinking models of G residues along the alginate chains. Thus, the optimal G residue content of the selected alginate, enables effective cross-linking of the matrix after printing process in a very stable and immediate way, allowing curation and ensuring the mechanical stability of the printed constructs. Consequently, the role of the alginate polymer included in the designed Alg-Lap formulation is not only convenient but essential. However, the described internal structure is affected mainly by the proportion of components used. As we have demonstrated with our results, the increase on the Lap concentration beyond 6 % (*w/v*) does have a great impact on the actual printability of

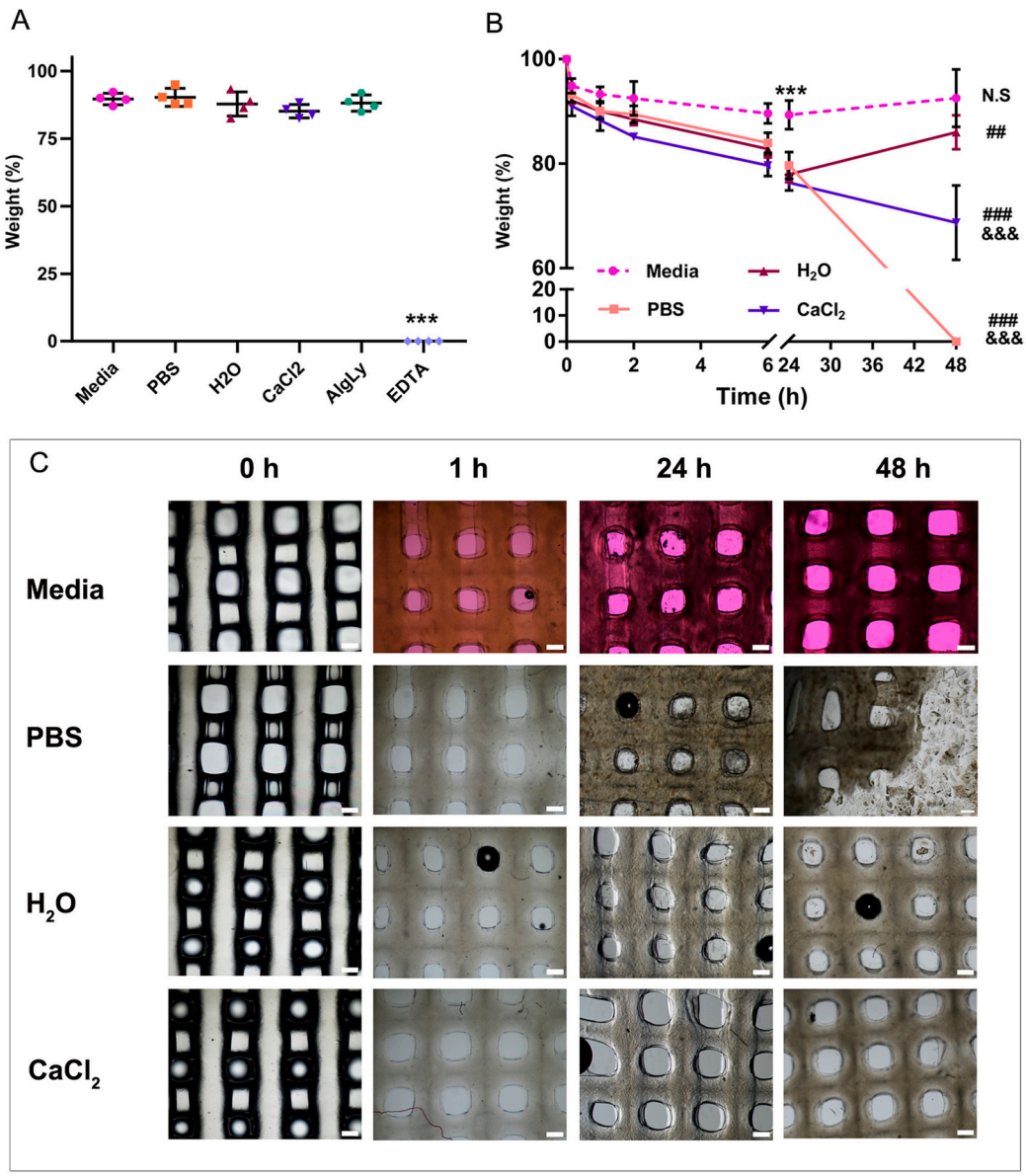

Fig. 7. Swelling and degradation profile of 3D constructs. Degradation (A) and Swelling (B) of Lap-Alg 3D printed constructs in different conditions over time. (Degradation: * represents comparison to their initial weight: $p < 0.001$ ***); (Swelling: * represents comparison between media all groups at 24 h: $p < 0.05$ *, $p < 0.01$ **, $p < 0.001$ ***; # represents the comparison between the weight (%) of each group at 48 h against their initial state: $p < 0.05$ # $p < 0.01$ ## $p < 0.001$ ###; & represents the comparison against media group at 48 h: $p < 0.001$ &&&). (C) Pictures of the internal pores for the swelling evaluation. Scale bar: 400 μm.

the matrix (Fig. 1A). Precisely, higher concentrations of nanoclay have demonstrated to elicit printing and shaping. Thus, in our study, a concentration of 6 % was stated as a maximum limit for printable Lap-Alg hydrogels. Consequently, appropriate hydrogel composition was stated for the 6 % Lap-Alg formulation manufactured within low ionic strength dispersion medium defined as miliQ H_2O.

In addition to complying with physicochemical characteristics necessary for EB3P technique, it is highly important to achieve reproducible printing processes that allow a reliable manufacture of biomedical products [35]. The inaccuracies observed in simple 2D geometries help to detect the parameters that would not be suitable for the printing of larger constructs. Thus, the screening among nozzle geometries, printing pressure and speed doubtlessly influences the uniformity, length and width of the printed strands [28,36,37]. As a first approach for hydrogel printability evaluation, we propose an easy and time saving 2D test. We screened the uniformity, fidelity and printing accuracy of the printed strands by assessing the deposition accuracy, spreading ratio and POI index obtained with different nozzle geometries, printing speeds and pressures. This allows to narrow down the most suitable printing parameters for the achievement of homogeneous, reproducible and well-shaped strands [23,36]. In our study, the use of conic nozzles lessens the uniformity, fidelity and accuracy of the strands printed with Lap-Alg ink, while increases their width due to over-extrusion (Fig. 2C, E). Besides, the employment of 2 mm/s speed and 75 kPa pressure with cylindrical nozzle generates uniform, reproducible and accurate strands. Moreover, the exact definition of the strand width in 2D assists to determine two parameters that are key to fabricate 3D constructs: the distance of the nozzle from the printing bed and the layer-height that should be determined to print 3D constructs layer-by-layer.

The transition from 2D printing to 3DP of multilayered constructs is a challenging process. In the case of hydrogel inks, this optimization requires an exhaustive evaluation since their high amount of water causes difficulties in layer stacking, leading to the collapse of the printed layers and the loss of their morphology. A good way to evaluate the stacking capacity and the morphological stability and accuracy of 3DP is the evaluation of the Printability Index (Pr). This parameter is directly related to the optimal printability of an ink [30,38,39]. However, Pr measurements are usually performed in a single layer prints, therefore dismissing the stacking behavior of the ink [30,40]. In our study, we propose the evaluation of Pr in our 3D constructs. This approach represents a notable advance in the evaluation of the printability of

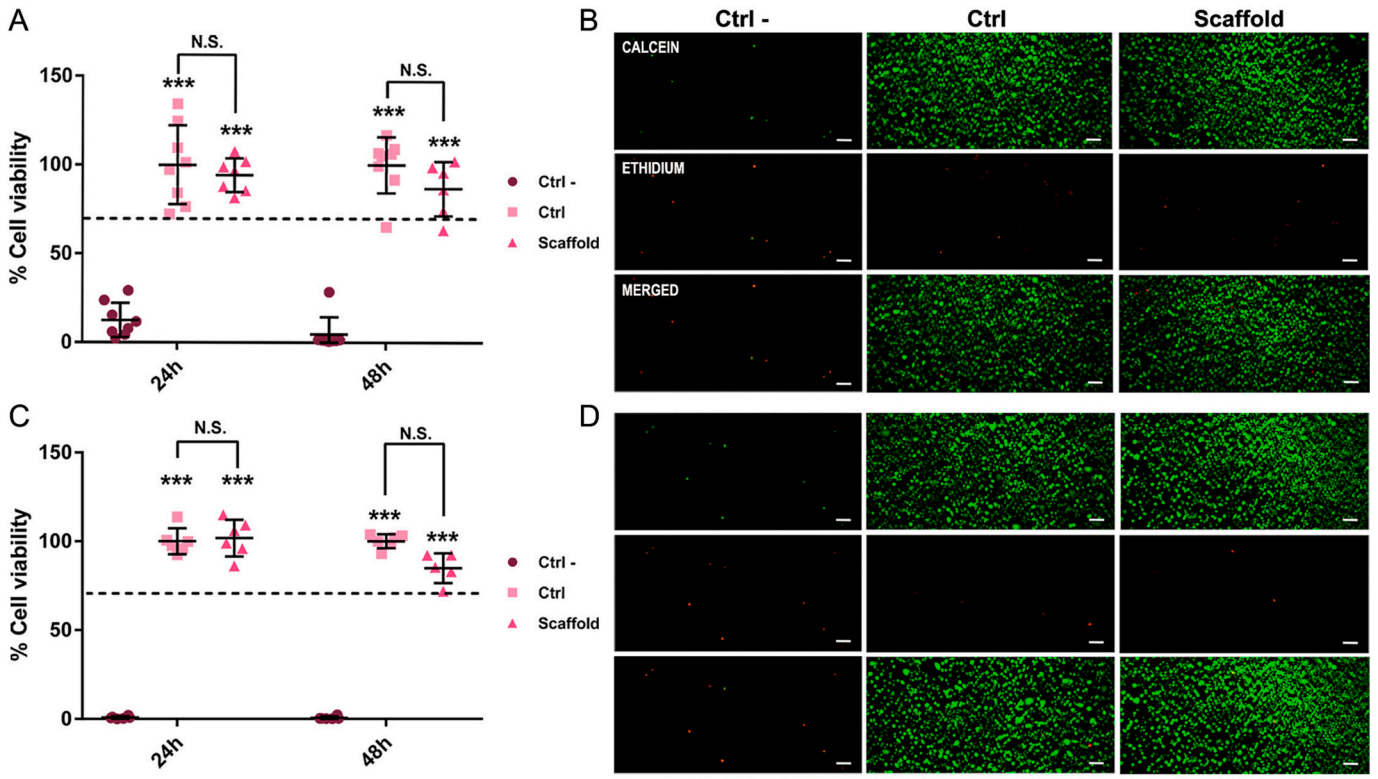

Fig. 8. Cytotoxicity assay of 3D printed scaffolds. (A-B) Extract cytotoxicity assay; L929 live/dead staining. (C—D) Indirect cytotoxicity assay; L929 live/dead staining. Scale bar: 200 μm. * represents comparison against Ctrl- group: $p < 0.05$ *, $p < 0.01$ **, $p < 0.001$ ***. N.S. non-significance.

hydrogels since it allows to verify that the set printed parameters, together with the optimized ink formulation ensure an excellent printability index, viscosity, and gelation with minimal strand collapse and good self-support [37,39,41] (Fig. 3B). As a remarkable novelty, this study provides a new tool for 3DP accuracy evaluation. Thus, we defined for the first time the 'Printing Accuracy Escalation Index' (PAEI). This parameter proves whether the printing accuracy observed with the selected parameters in 2D prints is scalable to 3D printed objects. In our study, the accuracy and shape fidelity of the outer geometry have endured excellently both in the fresh and crosslinked 5-layered and even 15-layered scaffolds (Fig. 5B) confirming the minimal diffusion of the printed strands in the internal pores and the self-support capacity of the ink (Fig. 3). All of these parameters contribute to unequal faithful printing process where computer design is accurately reproduced in printed constructs with solely a reasonable height deflection of the ink after subsequent layer deposition [28,41,42] (Fig. 5).

The perfect control of the printing process was validated by proving the ability to fabricate thick scaffolds (Fig. 3A) and complex structures (Fig. 6). The deposition versatility of this ink enabled to custom-tailor infill patterns ranging from simple straight lines to curved and hexagonal filament. Although creating tri-hexagons and curved filaments is highly complex, printing pattern adaptation has already been related to be suitable for a better biologic adaptation of constructs to final applications [43–45]. For instance, Honeycomb patterns have been employed for *in vitro* studies in hippocampal neurons [45][44]. Similarly, tri-hexagons and curved filaments have demonstrated to resemble microvasculature [24,46]. To the best of our knowledge, this is the first report that creates such a wide range of self-support infill structures with EB3P of hydrogels, which makes the designed Lap-Alg highly adaptive to several clinical applications.

Against all odds, when it comes to a 3D printed construct to be applied as a biomedical device, not only is the reproducibility of the manufacturing technique important, but also the stability of the final product obtained. Thus, it is of special relevance that the 3D constructs are able to maintain their shape and remain stable over time [24,25,47]. As it can be concluded in our mechanical characterization (Fig. 4), crosslinking times of 10 min is enough to obtain homogeneous and reproducible scaffolds over time, even among different batches.

Likewise, control over the obtained final printed products requires the prediction of its behavior when handled. Some of the potential applications of the scaffolds, in addition to *in vitro* experiments, might require suitable culture conditions for constructs. The incubation of the constructs in different commonly used conditions produces a deswelling in all the constructs during the first 24 h, regardless of the condition employed (Fig. 7B). This phenomena may be explained by the output of residual sodium after exfoliation of the nanoclay [31,48] (Fig. 10A). Briefly, Sodium ions are intercalated between dry Lap plates (Fig. 9A) and are commonly released on aqueous media provoking Lap exfoliation and gelification in a proposed structure named "house of cards" (Fig. 10B). Residuary sodium in the Lap-Alg hydrogel structure would exit the matrix depending on the Na^+ concentration of the surrounding media, dragging some water molecules during its exchange, therefore, decreasing the weight of the scaffold for the first 24 h. Once the exfoliation equilibrium is met swelling and degradation behavior of the matrix depends on media ionic composition. Thus, culture media maintains Alg crosslinked thanks to the presence of calcium ions on its composition. On the contrary lack of calcium ions of miliQ H_2O causes Alg crosslinking to disassemble eliciting swelling on the constructs. Similarly, lack of calcium on PBS media affects Alg chain interactions as well as phosphate interacts with Lap matrix to disentangle and causing its degradation. Ultimately, $CaCl_2$ reinforces Alg ionic crosslinking hardening and contracting the internal structure of the constructs causing their shrinkage and loss of weight (Fig. 7C; Suppl. Fig. 3). Similarly, the understanding of the hydrogel matrix structure and its ionic responsive behavior allowed us to develop an efficient construct degradation method for a quick and controlled scaffold disintegration employing EDTA dissolved in PBS where ions of the PBS attack the internal structure of the Lap and disrupt its ionic balance while Ca^{2+} ions

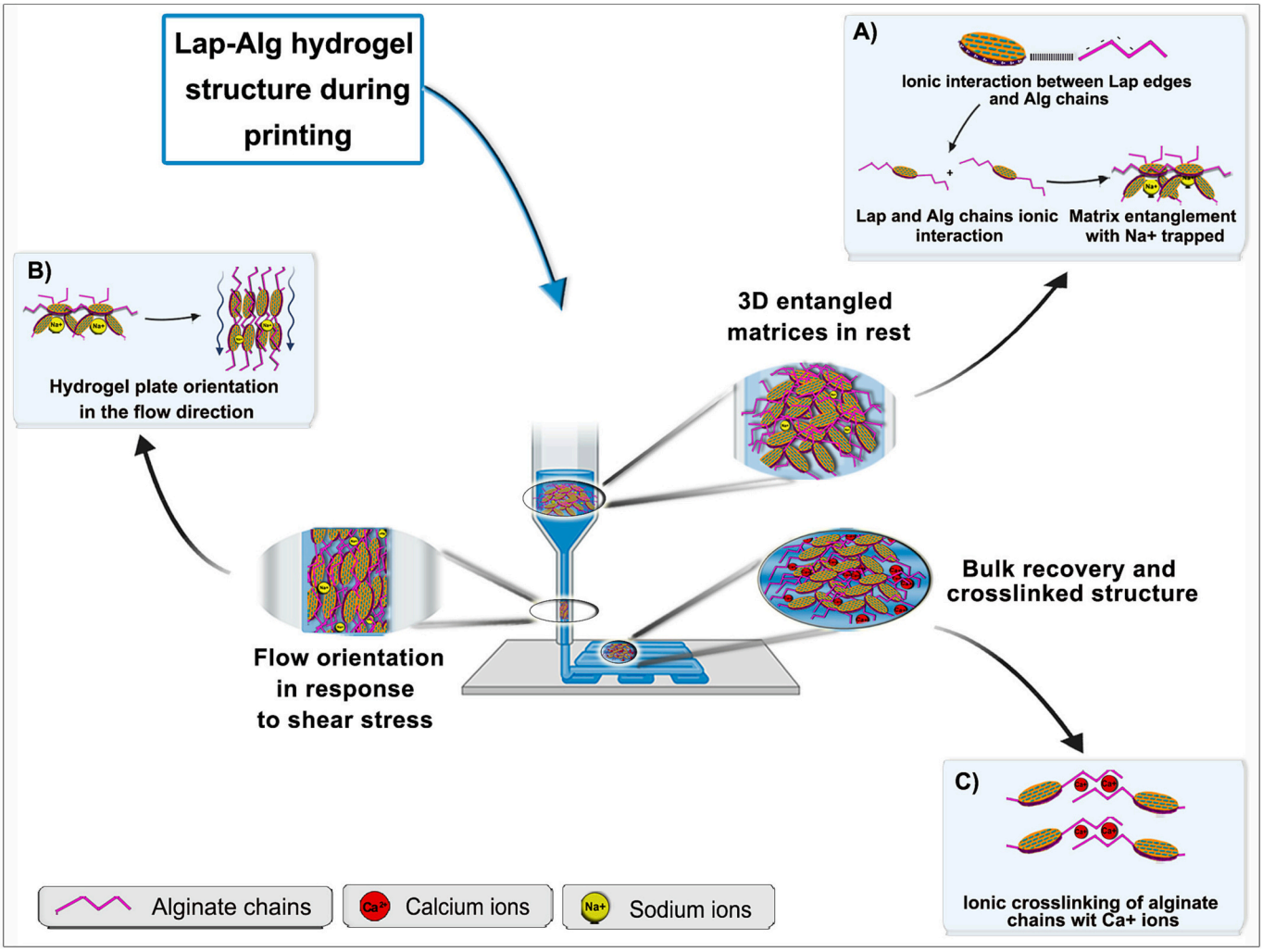

Fig. 9. Lap-Alg hydrogels structure during printing. (A) 3D entangled matrices in rest formed upon Lap and Alg ionic interactions. Entangled matrices assembled in rest when no pressure is applied in the printing cartridge. (B) Lap plates orientate in the flow direction when printing pressure is applied and shear forces act. (C) After printing rest state. Hydrogel matrix recovers the initial 3D assembling and curing process provides calcium ions crosslinking the matrix properly.

sequestering avoids Alg to reassemble crosslinked (Fig. 7A). Notably, degradation approaches involving mostly Alg chain degradation such as Alg Lyase enzymatic digestion was demonstrated to be inefficient, pointing Lap as a protective cover for enzyme cleaving sites of Alg and avoiding its degradation.

Finally, this research explores the cytotoxic effect of the manufactured devices. Although composites containing Lap have shown to be non-cytotoxic, the biocompatibility of this nanoclay when used as the main component of the hydrogels has not been considered in depth [17,18]. In our study, biocompatibility of a Lap-based formulation has been demonstrated, laying the bases for the employment of this nanoclay as a main character in composite printable materials.

5. Conclusions

In this article we propose the technological development of a hydrogel-based ink for EB3P that overcomes the problems attributed to hydrogel printing and demonstrates good printability and stability. The designed hydrogel-based inks have been evaluated by a battery of tests specifically selected for the quantitative and standardizable determination of the printability of the matrices providing a protocol for the evaluation of hydrogels as printable materials. This evaluation method allows to increase the efficiency and speed of printable hydrogel formulation development as well as its ideal adaptation to the 3D printing method. Notably, new printability evaluation methods have been proposed as an advance in the standardization of printable hydrogels obtaining process. As a result this protocol has enabled the highly precise and accurate printing of high and complex designs, achieving elevated shape-fidelity, stackability and resolution.

The development of this study involves obtaining a printable hydrogel that allows impeccable printing results and high resolution allowing to reproduce different infill patterns, as constructs with paramount potential for their employment in a wide range of biomedical applications.

In addition, this study not only demonstrates an organized and standardizable development of the formulations, but also an exhaustive study of them, thus giving rise to total control of the behavior of the printed constructs. Thus, the curation process of the obtained constructs with calcium chloride allows the long-term preservation of the printing outcomes obtained. This stability is maintained among different batches of printed constructs, which ensures reproducibility. Moreover, the printed constructs have been thoroughly evaluated in terms of mechanical behavior and biocompatibility proving their high potential for being used as biomedical devices. In addition, we propose the culture conditions that should be employed for the long-term maintenance of the printed scaffolds or their instant degradation, which allows full control over the constructs behavior for their adaptation into various applications.

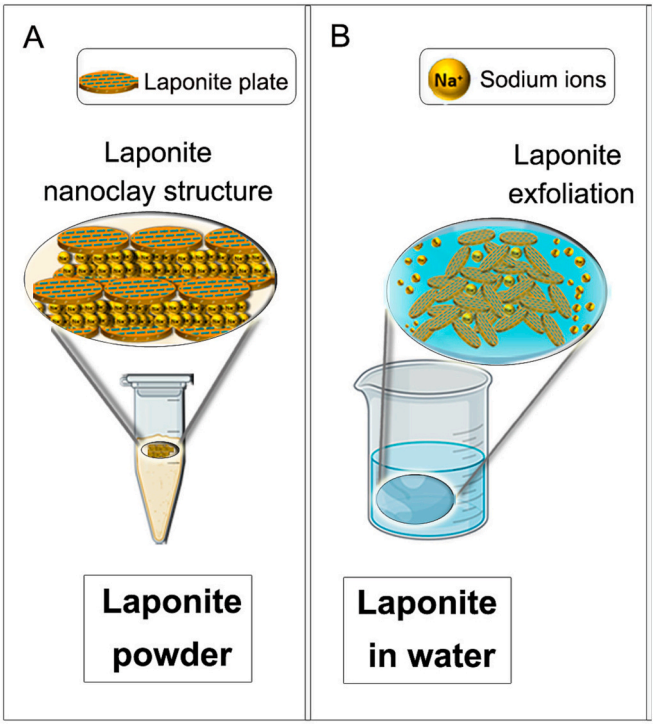

Fig. 10. Laponite powder structure and exfoliation. (A) Laponite dry powder structure stabilized with sodium ions interacted between nanoclay plates. (B) Laponite exfoliation in aqueous media. Sodium ions output through surrounding media and house of cards laponite matrix entanglement.

In conclusion, this entire development process has contributed to the standardization of the EB3P technique as well as to propose Lap-Alg hydrogel 3D printed constructs as promising applicative materials for biomedical applications.

Declaration of competing interest

The authors declare that they have no known competing financial interests or personal relationships that could have appeared to influence the work reported in this paper.

Data availability

The data that support the findings of this study are available upon reasonable request from the authors.

Acknowledgements

This project has been partially supported by Spanish government Ministerio de Ciencia e Innovación Grant PID2021-122577OB-I00 funded by MCIN/AEI/ 10.13039/501100011033 and by "ERDF A way of making Europe". Grant IT1448-22 funded by Basque Government and Fundación Vital Fundazioa (vital21/28). Elena Munoz-Perez thanks the Basque Government for the predoctoral grant (PRE_2022_2_0115). Arantza Perez-Valle thanks the Spanish Government for the postdoctoral grant (MARSA55/21).

Appendix A. Supplementary data

Supplementary data to this article can be found online at https://doi.org/10.1016/j.bioadv.2023.213414.

References

[1] G. Janarthanan, S. Lee, I. Noh, 3D printing of bioinspired alginate-albumin based instant gel ink with electroconductivity and its expansion to direct four-axis printing of hollow porous tubular constructs without supporting materials, Adv. Funct. Mater. 31 (45) (2021), 2104441, https://doi.org/10.1002/adfm.202104441.

[2] E. Munoz-Perez, A. Gonzalez-Pujana, M. Igartua, E. Santos-Vizcaino, R. M. Hernandez, Mesenchymal stromal cell secretome for the treatment of immune-mediated inflammatory diseases: latest trends in isolation, content optimization and delivery avenues, Pharmaceutics 13 (11) (2021), https://doi.org/10.3390/pharmaceutics13111802 doi:1802 [pii].

[3] J. Chakraborty, N. Majumder, A. Sharma, S. Prasad, S. Ghosh, 3D bioprinted silk-reinforced alginate-gellan gum constructs for cartilage regeneration, Bioprinting 28 (2022), e00232, https://doi.org/10.1016/j.bprint.2022.e00232.

[4] H. Kumar, K. Sakthivel, M.G.A. Mohamed, E. Boras, S.R. Shin, K. Kim, Designing gelatin methacryloyl (GelMA)-based bioinks for visible light stereolithographic 3D biofabrication, Macromol. Biosci. 21 (1) (2021), e2000317, https://doi.org/10.1002/mabi.202000317.

[5] Z. Jiang, B. Diggle, M.L. Tan, J. Viktorova, C.W. Bennett, L.A. Connal, Extrusion 3D printing of polymeric materials with advanced properties, Adv. Sci. 7 (17) (2020), 2001379, https://doi.org/10.1002/advs.202001379.

[6] Y. Liu, Q. Hu, W. Dong, S. Liu, H. Zhang, Y. Gu, Alginate/gelatin-based hydrogel with soy protein/peptide powder for 3D printing tissue-engineering scaffolds to promote angiogenesis, Macromol. Biosci. 22 (4) (2022), e2100413, https://doi.org/10.1002/mabi.202100413.

[7] M.C. Teixeira, N.S. Lameirinhas, J.P.F. Carvalho, A.J.D. Silvestre, C. Vilela, C.S. R. Freire, A guide to polysaccharide-based hydrogel bioinks for 3D bioprinting applications, Int. J. Mol. Sci. 23 (12) (2022), https://doi.org/10.3390/ijms23126564. doi:6564 [pii].

[8] K. Varaprasad, C. Karthikeyan, M.M. Yallapu, R. Sadiku, The significance of biomacromolecule alginate for the 3D printing of hydrogels for biomedical applications, Int. J. Biol. Macromol. 212 (2022) 561–578. S0141-8130(22)01141-2 [pii].

[9] G. Falcone, P. Mazzei, A. Piccolo, T. Esposito, T. Mencherini, R.P. Aquino, P. Russo, Advanced printable hydrogels from pre-crosslinked alginate as a new tool in semi solid extrusion 3D printing process, Carbohydr. Polym. 276 (2022), 118746. S0144-8617(21)01133-4 [pii].

[10] C. Del Amo, X. Fernandez-San Argimiro, M. Cascajo-Castresana, A. Perez-Valle, I. Madarieta, B. Olalde, I. Andia, Wound-microenvironment engineering through advanced-dressing bioprinting, Int. J. Mol. Sci. 23 (5) (2022), https://doi.org/10.3390/ijms23052836 doi:2836 [pii].

[11] J.L. Davila, M.A. d'Avila, Laponite as a rheology modifier of alginate solutions: physical gelation and aging evolution, Carbohydr. Polym. 157 (2017) 1–8. S0144-8617(16)31111-0 [pii].

[12] J.L. Dávila, M.A. d'Ávila, Rheological evaluation of laponite/alginate inks for 3D extrusion-based printing, Int. J. Adv. Manuf. Technol. 101 (1) (2019) 675–686, https://doi.org/10.1007/s00170-018-2876-y.

[13] F. Afghah, M. Altunbek, C. Dikyol, B. Koc, Preparation and characterization of nanoclay-hydrogel composite support-bath for bioprinting of complex structures, Sci. Rep. 10 (1) (2020) 5257, https://doi.org/10.1038/s41598-020-61606-x.

[14] B. Liu, J. Li, X. Lei, S. Miao, S. Zhang, P. Cheng, G. Pei, Cell-loaded injectable gelatin/alginate/LAPONITE(R) nanocomposite hydrogel promotes bone healing in a critical-size rat calvarial defect model, RSC Adv. 10 (43) (2020) 25652–25661, https://doi.org/10.1039/d0ra03040f.

[15] Z. Ma, H. He, C. Deng, Y. Ren, D. Lu, W. Li, J. Wang, 3D bioprinting of proangiogenic constructs with induced immunomodulatory microenvironments through a dual cross-linking procedure using laponite incorporated bioink, Compos. Part B 229 (2022), 109399, https://doi.org/10.1016/j.compositesb.2021.109399.

[16] F.F. Cai, S. Heid, A.R. Boccaccini, Potential of laponite(R) incorporated oxidized alginate-gelatin (ADA-GEL) composite hydrogels for extrusion-based 3D printing, J. Biomed. Mater. Res. B Appl. Biomater. 109 (8) (2021) 1090–1104, https://doi.org/10.1002/jbm.b.34771.

[17] L. Dong, Z. Bu, Y. Xiong, H. Zhang, J. Fang, H. Hu, X. Li, Facile extrusion 3D printing of gelatine methacrylate/laponite nanocomposite hydrogel with high concentration nanoclay for bone tissue regeneration, Int. J. Biol. Macromol. 188 (2021) 72–81. S0141-8130(21)01661-5 [pii].

[18] M. Sakhakarmy, S. Tian, L. Raymond, G. Xiong, J. Chen, Y. Jin, Printability study of self-supporting graphene oxide-laponite nanocomposites for 3D printing applications, Int. J. Adv. Manuf. Technol. 114 (1) (2021) 343–355, https://doi.org/10.1007/s00170-021-06870-5.

[19] T. Ahlfeld, G. Cidonio, D. Kilian, S. Duin, A.R. Akkineni, J.I. Dawson, M. Gelinsky, Development of a clay based bioink for 3D cell printing for skeletal application, Biofabrication 9 (3) (2017), https://doi.org/10.1088/1758-5090/aa7e96, 034103–5090/aa7e96.

[20] C. Boyer, L. Figueiredo, R. Pace, J. Lesoeur, T. Rouillon, C.L. Visage, G. Rethore, Laponite nanoparticle-associated silated hydroxypropylmethyl cellulose as an injectable reinforced interpenetrating network hydrogel for cartilage tissue engineering, Acta Biomater. 65 (2018) 112–122, https://doi.org/10.1016/j.actbio.2017.11.027.

[21] M. Kazemzadeh-Narbat, J. Rouwkema, N. Annabi, H. Cheng, M. Ghaderi, B. Cha, A. Khademhosseini, Engineering photocrosslinkable bicomponent hydrogel constructs for creating 3D vascularized bone, Adv. Healthc. Mater. 6 (10) (2017), https://doi.org/10.1002/adhm.201601122. Epub 2017 Feb 27.

[22] A.C. Daly, S.E. Critchley, E.M. Rencsok, D.J. Kelly, A comparison of different bioinks for 3D bioprinting of fibrocartilage and hyaline cartilage, Biofabrication 8 (4) (2016), https://doi.org/10.1088/1758-5090/8/4/045002, 045002–5090/8/4/045002.
[23] B. Webb, B.J. Doyle, Parameter optimization for 3D bioprinting of hydrogels, Bioprinting 8 (2017) 8–12, https://doi.org/10.1016/j.bprint.2017.09.001.
[24] S. Naghieh, X. Chen, Printability-a key issue in extrusion-based bioprinting, J. Pharm.Anal. 11 (5) (2021) 564–579, https://doi.org/10.1016/j.jpha.2021.02.001.
[25] M.D. Giuseppe, N. Law, B. Webb, A.R. Macrae, L.J. Liew, T.B. Sercombe, B. J. Doyle, Mechanical behaviour of alginate-gelatin hydrogels for 3D bioprinting, J. Mech. Behav. Biomed. Mater. 79 (2018) 150–157. S1751-6161(17)30562-3 [pii].
[26] A. Habib, V. Sathish, S. Mallik, B. Khoda, 3D printability of alginate-carboxymethyl cellulose hydrogel, Materials 11 (3) (2018), https://doi.org/10.3390/ma11030454 doi:E454 [pii].
[27] N. Paxton, W. Smolan, T. Bock, F. Melchels, J. Groll, T. Jungst, Proposal to assess printability of bioinks for extrusion-based bioprinting and evaluation of rheological properties governing bioprintability, Biofabrication 9 (4) (2017), https://doi.org/10.1088/1758-5090/aa8dd8, 044107–5090/aa8dd8.
[28] G. Gillispie, P. Prim, J. Copus, J. Fisher, A.G. Mikos, J.J. Yoo, S.J. Lee, Assessment methodologies for extrusion-based bioink printability, Biofabrication 12 (2) (2020), https://doi.org/10.1088/1758-5090/ab6f0d, 022003–5090/ab6f0d.
[29] A. Schwab, R. Levato, M. D'Este, S. Piluso, D. Eglin, J. Malda, Printability and shape fidelity of bioinks in 3D bioprinting, Chem. Rev. 120 (19) (2020) 11028–11055, https://doi.org/10.1021/acs.chemrev.0c00084.
[30] H. Li, Y.J. Tan, S. Liu, L. Li, Three-dimensional bioprinting of oppositely charged hydrogels with super strong interface bonding, ACS Appl. Mater. Interfaces 10 (13) (2018) 11164–11174, https://doi.org/10.1021/acsami.7b19730.
[31] N. Sallstrom, A. Capel, M.P. Lewis, D.S. Engstrom, S. Martin, 3D-printable zwitterionic nano-composite hydrogel system for biomedical applications, J.Tissue Eng. 11 (2020), https://doi.org/10.1177/2041731420967294, 2041731420967294.
[32] T. Gao, G.J. Gillispie, J.S. Copus, A.K. Pr, Y.J. Seol, A. Atala, S.J. Lee, Optimization of gelatin-alginate composite bioink printability using rheological parameters: a systematic approach, Biofabrication 10 (3) (2018), https://doi.org/10.1088/1758-5090/aacdc7, 034106–5090/aacdc7.
[33] T.B. Becher, C.B. Braga, D.L. Bertuzzi, M.D. Ramos, A. Hassan, F.N. Crespilho, C. Ornelas, The structure-property relationship in LAPONITE(R) materials: from wigner glasses to strong self-healing hydrogels formed by non-covalent interactions, Soft Matter 15 (6) (2019) 1278–1289, https://doi.org/10.1039/c8sm01965g.
[34] T. Nicolai, S. Cocard, Dynamic light-scattering study of aggregating and gelling colloidal disks, J. Colloid Interface Sci. 244 (1) (2001) 51–57, https://doi.org/10.1006/jcis.2001.7930.
[35] F. Puza, K. Lienkamp, 3D printing of polymer hydrogels—from basic techniques to programmable actuation, Adv. Funct. Mater. n/a (2022), 2205345, https://doi.org/10.1002/adfm.202205345.
[36] F.E. Freeman, D.J. Kelly, Tuning alginate bioink stiffness and composition for controlled growth factor delivery and to spatially direct MSC fate within bioprinted tissues, Sci. Rep. 7 (1) (2017), 17042-1, https://doi.org/10.1038/s41598-017-17286-1.
[37] S. Gerdes, S. Ramesh, A. Mostafavi, A. Tamayol, I.V. Rivero, P. Rao, Extrusion-based 3D (bio)printed tissue engineering scaffolds: process–structure–quality relationships, ACS Biomater.Sci.Eng. 7 (10) (2021) 4694–4717, https://doi.org/10.1021/acsbiomaterials.1c00598.
[38] N. Soltan, L. Ning, F. Mohabatpour, P. Papagerakis, X. Chen, Printability and cell viability in bioprinting alginate dialdehyde-gelatin scaffolds, ACS Biomater.Sci. Eng. 5 (6) (2019) 2976–2987, https://doi.org/10.1021/acsbiomaterials.9b00167.
[39] A.S. Theus, L. Ning, B. Hwang, C. Gil, S. Chen, A. Wombwell, V. Serpooshan, Bioprintability: physiomechanical and biological requirements of materials for 3D bioprinting processes, Polymers 12 (10) (2020), https://doi.org/10.3390/polym12102262 doi:E2262 [pii].
[40] L. Ouyang, R. Yao, Y. Zhao, W. Sun, Effect of bioink properties on printability and cell viability for 3D bioplotting of embryonic stem cells, Biofabrication 8 (3) (2016), https://doi.org/10.1088/1758-5090/8/3/035020, 035020–5090/8/3/035020.
[41] A. Ribeiro, M.M. Blokzijl, R. Levato, C.W. Visser, M. Castilho, W.E. Hennink, J. Malda, Assessing bioink shape fidelity to aid material development in 3D bioprinting, Biofabrication 10 (1) (2017), https://doi.org/10.1088/1758-5090/aa90e2, 014102–5090/aa90e2.
[42] G. Ahn, K.H. Min, C. Kim, J.S. Lee, D. Kang, J.Y. Won, J.H. Shim, Precise stacking of decellularized extracellular matrix based 3D cell-laden constructs by a 3D cell printing system equipped with heating modules, Sci. Rep. 7 (1) (2017) 8624–8625, https://doi.org/10.1038/s41598-017-09201-5.
[43] C. Du, J. Hu, X. Wu, H. Shi, H.C. Yu, J. Qian, Q. Zheng, 3D printing of a tough double-network hydrogel and its use as a scaffold to construct a tissue-like hydrogel composite, J.Mater.Chem.B 10 (3) (2022) 468–476, https://doi.org/10.1039/d1tb02465e.
[44] Y. Wu, A. Wenger, H. Golzar, X.S. Tang, 3D bioprinting of bicellular liver lobule-mimetic structures via microextrusion of cellulose nanocrystal-incorporated shear-thinning bioink, Sci. Rep. 10 (1) (2020), 20648-3, https://doi.org/10.1038/s41598-020-77146-3.
[45] Q. Zhang, X. Yang, P. Li, G. Huang, S. Feng, C. Shen, T.J. Lu, Bioinspired engineering of honeycomb structure – using nature to inspire human innovation, Prog. Mater. Sci. 74 (2015) 332–400, https://doi.org/10.1016/j.pmatsci.2015.05.001.
[46] J.E. Snyder, Q. Hamid, C. Wang, R. Chang, K. Emami, H. Wu, W. Sun, Bioprinting cell-laden matrigel for radioprotection study of liver by pro-drug conversion in a dual-tissue microfluidic chip, Biofabrication 3 (3) (2011), https://doi.org/10.1088/1758-5082/3/3/034112, 034112-5082/3/3/034112. Epub 2011 Sep 1.
[47] Z. Wang, Viscoelastic properties of cardiovascular tissues (pp. Ch. 7), in: Mark J. Golob (Ed.), Viscoelastic and Viscoplastic Materials, IntechOpen, Rijeka, 2016. doi:10.5772/64169 Retrieved from doi:10.5772/64169.
[48] G.A. Valencia, M. Djabourov, F. Carn, P.J.A. Sobral, Novel insights on swelling and dehydration of laponite, Colloid Interface Sci.Commun. 23 (2018) 1–5, https://doi.org/10.1016/j.colcom.2018.01.001.